

Phenomenology of Neutrino-Dark Matter Interaction in DSNB and AGN

Po-Yan Tseng¹ and Yu-Min Yeh¹

¹ *Department of Physics and CTC, National Tsing Hua University, Hsinchu 300, Taiwan*

ABSTRACT: We introduce a neutrino-scalar dark matter (DM) ν - ϕ interaction and consider Diffuse Supernova Neutrino Background (DSNB) and Active Galactic Nuclei (AGN) representing distinctive neutrino sources. We focus on interaction mediated by a heavy fermionic particle F and investigate the attenuation of neutrino fluxes from these sources. We model the unscattered neutrino flux from DSNB via core-collapse supernova (CCSN) and star-formation rate (SFR), then use the DUNE experiment to set limits on DM-neutrino interaction. For AGNs, NGC 1068 and TXS 0506+056 where the neutrino carries energy above TeV, we select the kinematic region $m_F^2 \gg E_\nu m_\phi \gg m_\phi^2$ such that the $\nu\phi$ scattering cross section features an enhancement at high energy. We investigate the constraint on m_ϕ and scattering cross section by including DM density spikes at center of AGNs and computing the neutrino flux at IceCube, where the $\phi\phi^*$ annihilation cross section is implemented to obtain the saturation density of the spikes.

Contents

1	Introduction	1
2	Scalar Dark Matter-Neutrino Interactions	2
3	Diffuse Supernova Neutrino Background and DUNE Experiment	4
4	Active Galactic Nuclei NGC 1068 and TXS 0506+056	6
5	Conclusion	10
A	Calculation of Cross Section	12
B	The Detail Calculation of νAr Scattering	13
C	Calculation for ρ_0 and r_0	14

1 Introduction

Dark Matter (DM), accounts for 27% of the Universe, is yet identified from particle physics point of view. DM particles are hardly detected in the lab if they have only revealed the interaction with Standard Model (SM) particles through gravity which provided indirect evidence of DM in cosmological scale. Many observations have been proposed to study the imprints of fundamental interaction between DM and Standard Model (SM) particles, such as the cosmological and astrophysical effects on various hypothetical DM interactions [1–4], or the boosted DM scenarios where non-relativistic DM particles gain energy through the upper scattering with cosmic electrons or neutrinos [5–8].

In this work, we focus on the hypothetical interaction between scalar DM ϕ and neutrino then study the phenomenological outcome. In particular, we introduce fermion-mediated interactions in Section 2, where the $\nu\phi$ scattering cross section $\sigma_{\nu\phi}$ follows different neutrino energy dependence according to various kinematic regions. For example, in the limit $E_\nu \gg m_\phi \simeq m_F$, $\sigma_{\nu\phi}$ is inversely proportional to E_ν , and thus the low neutrino sources are more applicable. On the other hand, in the heavy mediator limit, $m_F^2 \gg E_\nu m_\phi \gg m_\phi^2$, the $\sigma_{\nu\phi} \propto E_\nu$ exhibits enhancement at high energy. Therefore, we consider two neutrinos sources: The Diffuse Supernova Neutrino Background (DSNB) and the Active Galactic Nuclei (AGN). These two special sources provide prolific neutrinos with energy of $\mathcal{O}(10 \text{ MeV})$ and $\mathcal{O}(100 \text{ TeV})$, respectively. The existence of neutrino-DM interactions would manifest from attenuating the neutrino flux during the propagation from the sources to the Earth.

The anticipated DSNB originating from the distant Core-Collapse SuperNova (CCSN) is not yet observed by the current neutrino detectors. It is pointed out that it can be potentially observed at Super-Kamiokande/Hyper-Kamiokande (SK/HK) [9–12]. In Section 3, we model the DSNB flux of electron neutrino via a thermal non-degenerate Fermi-Dirac distribution with temperature 6.6 MeV [11] and focus on the open energy region of $\mathcal{O}(10)$ MeV sandwiched by the overwhelming backgrounds expected at the future neutrino detectors (i.e reactor $\bar{\nu}_e$ from beta decay and ν_e from inverse muon decay). The DSNB flux depends on the rate of CCSN, which relates to the history of Star-Formation Rate (SFR). We compute the DSNB flux via including the effect of $\nu\phi$ scattering, and perform the sensitivity analysis by introducing the Deep Underground Neutrino Experiment (DUNE). The DUNE is the future neutrino detection project and aims to investigate various topics in neutrino physics, such as neutrino oscillations, baryon number violation, supernova neutrino bursts, etc. [13, 14] To obtain corresponding event number from DSNB, we calculate the MeV neutrino-Argon, $\nu_e\text{Ar}$, scattering rate and estimate the sensitivity on $\nu\text{-}\phi$ coupling y .

AGNs are considered as alternative sources emit neutrinos above $\mathcal{O}(\text{TeV})$, which is ideal to probe the kinematic region where the neutrino-DM cross section increases with energy. The IceCube Collaboration has observed the ultra high energy neutrinos from the galaxies, NGC 1068 and TXS 0506+056 [15–17]. It was assumed in earlier works [18–20] that AGN possess a spike-like DM density profile around the center SuperMassive Black Holes (SMBH). Furthermore, this profile, especially the saturation DM density, is directly associated with the DM self annihilation. It is legitimate to assume emitted neutrinos interact intensively with the DM around the SMBH, which increases the neutrino attenuation. Considering the interplay between the $\nu\phi$ scattering and the $\phi\phi^*$ annihilation cross sections on NGC 1068 and TXS 0506+056, we demonstrate the upper bounds on $\nu\phi$ interaction in Section 4.

We conclude our results in Section 5 and show the detailed calculations for scattering cross sections and spike-like density parameters in appendices.

2 Scalar Dark Matter-Neutrino Interactions

We consider neutrino as Majorana fermion which couples to scalar DM ϕ through a fermionic mediator F [21]:

$$\mathcal{L}_{F\text{-med}} = y(\phi\bar{\nu}_L F_R + \phi^*\bar{F}_R\nu_L), \quad (2.1)$$

where y is the coupling constant. Here, we adopt the “non-self conjugate” DM ($\phi \neq \phi^*$) case. Because the “self-conjugate” dark scalar ($\phi = \phi^*$) does not contribute to the elastic scattering with neutrinos, but “non-self conjugate” case has u -channel contribution. The total cross section of $\nu\phi$ scattering is given in Appendix A, Eq. (A.4). The neutrino-DM scattering cross section from Eq. (2.1) exhibits different energy dependent. For instance, when the neutrino energy E_ν is much smaller than the DM mass m_ϕ and the mediator

mass m_F , we have

$$\sigma_{\nu\phi} \simeq \frac{y^4 E_\nu^2}{16\pi(m_F^2 - m_\phi^2)^2} \quad (2.2)$$

in case of $m_F > m_\phi$. For $m_F = m_\phi \gg E_\nu$, the cross section becomes

$$\sigma_{\nu\phi} \simeq \frac{y^4}{64\pi m_\phi^2}, \quad (2.3)$$

which becomes energy independent. In contrast, for $E_\nu \gg m_{\phi,F}$, it can be approximated as

$$\sigma_{\nu\phi} = \frac{y^4}{64\pi} \left[\frac{\ln\left(1 + \frac{2E_\nu m_\phi}{m_F^2}\right) - 1}{E_\nu m_\phi} \right] \sim E_\nu^{-1}. \quad (2.4)$$

Another useful limit is when $m_F^2 \gg E_\nu m_\phi \gg m_\phi^2$, the cross section becomes linear in E_ν :

$$\sigma_{\nu\phi} \simeq \sigma_0 \frac{E_\nu}{E_0}, \quad \text{where } \sigma_0 \equiv \left(\frac{y^4 m_\phi}{32\pi m_F^4} \right) E_0. \quad (2.5)$$

and E_0 is a arbitrary rescale energy.

For DSNB, the neutrinos are emitted with energy scale of $\mathcal{O}(\text{MeV})$. In this case, we choose similar masses of m_ϕ and m_F , in particular fixing $m_F/m_\phi = 1.1$ to avoid divergence in Eq. (2.2), and examine the relations between y and m_ϕ . On the other hand, considering $\mathcal{O}(\text{TeV})$ neutrino sources, for instance AGN, the $\nu\phi$ scattering cross section with linear energy dependent is more applicable. The aforementioned interactions cause the deduction of the anticipated neutrino fluxes at detectors, say DUNE or IceCube, which we will further discuss in the following sections.

To quantify the flux attenuation from distance neutrino sources, we need to calculate the transmittance T , defined as the ratio of the received and the emitted flux, which can be obtained from the optical depth τ [22]

$$T = e^{-\tau}, \quad \text{where } \tau(E_\nu, z) = \int_0^z \frac{\Gamma(E_\nu, z')}{(1+z')H(z')} dz', \quad (2.6)$$

and scattering rate $\Gamma = \sigma_{\nu\phi} n_{\text{DM}}$. The extragalactic averaged DM density is $n_{\text{DM}} = 1.27 \text{ GeV m}^{-3}$. Here, the upper and lower integral limits associate with the redshifts of neutrino source and observer, respectively. With the redshift at z' included, we must replace E_ν , the incident neutrino energy at today, by $E_\nu(1+z')$ and n_{DM} by $n_{\text{DM}}(1+z')^3$. The Hubble rate at matter-dominating epoch is given by

$$H(z) = H_0 \sqrt{\Omega_m(1+z)^3 + \Omega_\Lambda} \quad (2.7)$$

with $H_0 = 67.36 \text{ km s}^{-1} \text{ Mpc}^{-1}$ and $\Omega_m = 0.3153$, $\Omega_\Lambda = 0.6847$ are the matter and vacuum contributions to the energy density [23, 24].

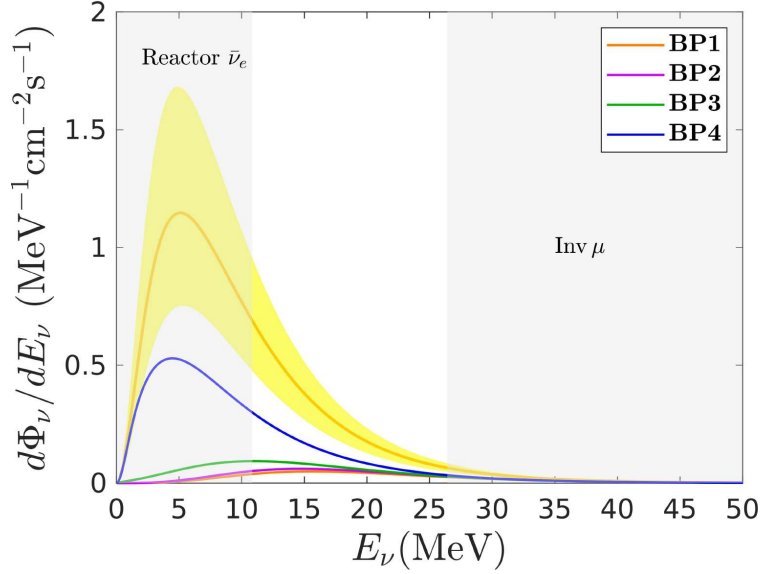


Figure 1: The DSNB flux for electron neutrino ν_e with temperature $T_\nu = 6.6$ MeV (dark yellow) and the fluxes of **BPs** in Table 1 including DM attenuation. The yellow shaded region indicates the uncertainties arising from SFR. The gray shaded regions are the backgrounds of Reactor $\bar{\nu}_e$ and $\text{Inv } \mu$.

3 Diffuse Supernova Neutrino Background and DUNE Experiment

The DSNB models isotropic neutrino and antineutrino sources from core-collapse supernovae. The distribution of neutrino emitted from a supernova has the following Fermi-Dirac form [9]:

$$F_\nu(E_\nu) = \frac{E_\nu^{\text{tot}}}{6} \frac{120 E_\nu^2}{7\pi^4 T_\nu^4} \frac{1}{\exp(E_\nu/T_\nu) + 1}, \quad (3.1)$$

where $E_\nu^{\text{tot}} = 3 \times 10^{53}$ erg is the total emitted energy (1/6 factor stands for energy of one of $\nu_e, \nu_{\bar{e}}, \nu_\mu, \nu_{\bar{\mu}}, \nu_\tau, \nu_{\bar{\tau}}$) and T_ν is the neutrino temperature. The diffuse differential neutrino flux without DM attenuation is given by

$$\frac{d\Phi_\nu}{dE_\nu} = \int_0^{z_{\text{max}}} \frac{R_{\text{CCSN}}(z) F_\nu(E_\nu, z)}{H(z)} dz. \quad (3.2)$$

The rate R_{CCSN} and the SFR parameters are [10, 25]

$$R_{\text{CCSN}}(z) = \dot{\rho}_*(z) \frac{\int_{8M_\odot}^{50M_\odot} \psi(M) dM}{\int_{0.1M_\odot}^{100M_\odot} M \psi(M) dM}, \quad (3.3a)$$

$$\dot{\rho}_*(z) = \dot{\rho}_0 \left[(1+z)^{-10\alpha} + \left(\frac{1+z}{B} \right)^{-10\beta} + \left(\frac{1+z}{C} \right)^{-10\gamma} \right]^{-1/10}, \quad (3.3b)$$

where $B = 2^{1-\alpha/\beta}$, $C = 2^{(\beta-\alpha)/\gamma} \cdot 5^{1-\beta/\gamma}$, $\dot{\rho}_0 = 0.0178_{-0.0036}^{+0.0035} M_\odot \text{ yr}^{-1} \text{ Mpc}^{-3}$, and $\alpha = 3.4 \pm 0.2$, $\beta = -0.3 \pm 0.2$, $\gamma = -3.5 \pm 1$. The initial mass function $\psi(M)$ is proportional to

	BP1	BP2	BP3	BP4
m_ϕ/GeV	4.27×10^{-6}	1.03×10^{-4}	1.06×10^{-2}	3.15×10^{-1}
y	4.29×10^{-2}	2.30×10^{-1}	3.39	45.04

Table 1: Parameter values of **BPs** in Fig. 1 and Fig. 2.

$M^{-2.35}$ [26]. We demonstrate the flux of ν_e with $T_\nu = 6.6$ MeV in Fig. 1 with dark yellow curve, and the yellow shaded region represents the uncertainties from SFR.

To include the scattering of neutrinos and dark scalar ϕ , we add the transmittance T into Eq. (3.2):

$$\frac{d\Phi_\nu}{dE_\nu} = \int_0^{z_{\max}} \frac{R_{\text{CCSN}}(z) F_\nu(E_\nu, z) T(E_\nu, z)}{H(z)} dz. \quad (3.4)$$

We fixed $z_{\max} = 5$ for which there is a reasonable amount of star formation.

To detect DSNB on Earth, we consider the deep underground neutrino experiment (DUNE), which provides the charged current interaction of liquid argon and low energy electron neutrino:

$$\nu_e + {}^{40}\text{Ar} \rightarrow e^- + {}^{40}\text{K}^*. \quad (3.5)$$

The neutrino incident energy can be written as

$$E_\nu = E_e + [(m_{\text{K}}^g + E_x) - m_{\text{Ar}}^g] + T_{\text{K}}, \quad (3.6)$$

where E_e is the energy of outgoing electron, m_{K}^g (m_{Ar}^g) is the ground-state mass of potassium (argon), E_x is the excitation energy, and T_{K} is the recoil kinetic energy of K. For low energy neutrinos, one may neglect T_{K} . The mass difference $m_{\text{K}}^g - m_{\text{Ar}}^g$ is around 1.505 MeV. The total ν -Ar cross section $\sigma_{\nu\text{Ar}}$ of this interaction in the CM frame is given in Appendix B, where we use the data set of the nuclear matrix elements from Ref. [27]. By assuming 400 kton-years of exposure of a DUNE detector, we may calculate the numbers of event of the scattering Eq. (3.5). The event number is given by

$$N(E_e) = \epsilon N_{\text{Ar}} \int dE_\nu \frac{d\Phi_\nu}{dE_\nu} \sigma_{\nu\text{Ar}}, \quad (3.7)$$

where ϵ is the detector efficiency and is assumed to be 100%, N_{Ar} is the number of target argon. The binned event number of the DSNB flux is shown in the left panel of Fig. 2. The uncertainty including the systematic and statistic errors (blue shaded region) of each bin i is determined by

$$\sigma_i^{\text{tot}} = \sqrt{(\sigma_i^{\text{sys}})^2 + N_i}, \quad \text{where } \sigma_i^{\text{sys}} = \frac{N_i^+ - N_i^-}{2}. \quad (3.8)$$

N_i , N_i^+ and N_i^- are the event numbers for the DSNB fluxes with fiducial, upper, and lower SFR parameters.

From Eq. (3.4) we can calculate the event number of the scattered DSNB flux and recast to constraint on m_ϕ and y by the χ^2 test

$$\chi^2 = \sum_i \left[\frac{N_i - N_i^{\text{sct}}}{\sigma_i^{\text{tot}}} \right]^2 \leq 4, \quad (3.9)$$

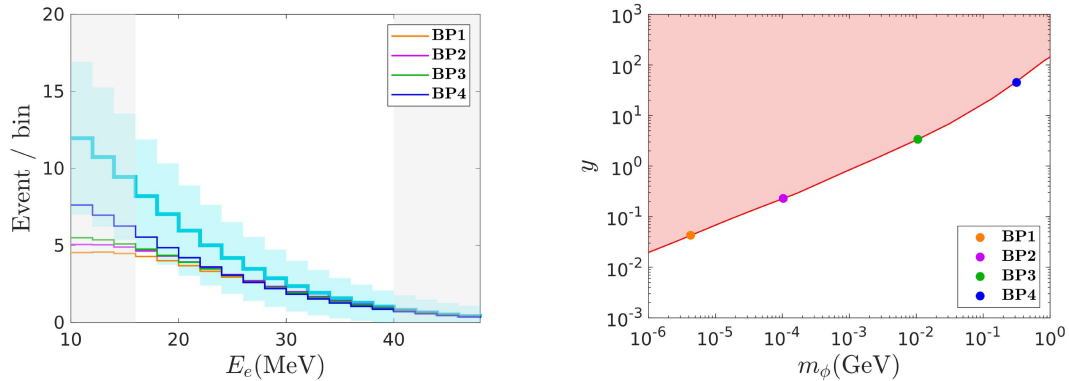


Figure 2: (left) The event number for the DSNB flux with $T_\nu = 6.6$ MeV as a function of electron energy and the corresponding event numbers of benchmark points. The gray shaded areas do not contribute to χ^2 value due to the overwhelming background events [28]. (right) Projecting sensitivity on m_ϕ and y given by the χ^2 test. The corresponding values of **BPs** are listed in Table 1.

where N_i^{sct} is the event numbers computed from Eq. (3.7) and Eq. (3.4). To obtain the conservative bounds, we adopted the 1σ upper values of SFR parameters to calculate CCSN, and scanned over the parameter space

$$10^{-6} \leq m_\phi/\text{GeV} \leq 1, \quad 10^{-3} \leq y \leq 10^3 \quad (3.10)$$

to calculate transmittance T . Notice that, the bins belong to the gray shaded areas in the left panel of Fig. 2 do not contribute to χ^2 in Eq. (3.9). We fixed $m_F/m_\phi = 1.1$ in our analysis, and the sensitivity is shown in the right panel of Fig. 2 by the red curve where the above region is disfavoured by 2σ . The coupling constant in the excluded red region is too large so that the neutrinos and dark scalar scatter intensively, hence the corresponding flux is too small to produce enough event number of ν_e -Ar scattering at DUNE. In Fig. 2, the y value increases as m_ϕ increases, this is because the cross section is inversely proportional to the DM mass and mediator mass according to Eq. (2.2) and (2.4). Since $\sigma_{\nu\phi} \propto m_\phi^{-1}$ in $m_\phi/\text{GeV} \lesssim 10^{-3}$ and $\sigma_{\nu\phi} \propto m_\phi^{-4}$ in $m_\phi/\text{GeV} \gtrsim 10^{-1}$, the slope of the margin is slightly increased. There are four selected benchmark points on the margin. The event numbers of each **BP** were significantly attenuated at low electron recoil energy. The corresponding DSNB fluxes of **BPs** are also shown in Fig. 1. There is an open energy window from 10.8 MeV to 26.4 MeV which is sandwiched by the overwhelming backgrounds of reactor $\bar{\nu}_e$ and inverse μ decay. We can see that all of the **BPs** can be distinguished from the unattenuated DSNB flux and produce the detectable suppression signal.

4 Active Galactic Nuclei NGC 1068 and TXS 0506+056

AGNs of NGC 1068 and TXS 0506+056 produce ultra high-energy neutrinos have been detected at IceCube [15, 16]. It was suggested that the DM density around the SMBH at

	NGC BP1	NGC BP2	NGC BP3	NGC BP4
m_ϕ/GeV	2.63×10^{-5}	8.94×10^{-4}	1.81×10^{-2}	5.34×10^{-1}
σ_0/cm^2	3.01×10^{-37}	3.74×10^{-35}	3.35×10^{-32}	9.94×10^{-29}
$\langle\sigma_{\phi\phi}v\rangle/\text{cm}^2$	1.05×10^{-51}	4.46×10^{-48}	8.08×10^{-44}	7.08×10^{-39}

Table 2: Parameter values of NGC BPs in Fig. 3.

the center of an AGN, for $r \leq R_{\text{sp}}$, may form a spike, which is given by [19]

$$\rho_{\text{sp}} = \rho_{Rg_\gamma}(r) \left(\frac{R_{\text{sp}}}{r} \right)^{\gamma_{\text{sp}}}, \quad (4.1)$$

where [20]

$$R_{\text{sp}} = \frac{M_{\text{BH}}}{4\pi\rho_0 r_0 [f(r_h) - f(r_i)]} \quad (4.2)$$

represents the size of the spike, r_h is the influence radius of supermassive black hole [29], and r_i is the inner radius of the spike here we take it to be four times the Schwarzschild radius, i.e. $r_i = 4R_s$ [19]. In addition, we take the DM self annihilation into account, the density Eq. (4.1) should be modified by

$$\frac{\rho_{\text{sp}}(r)\rho_{\text{sat}}}{\rho_{\text{sp}}(r) + \rho_{\text{sat}}} \quad (4.3)$$

which reaches the saturation density (refer Appendix C for more details)

$$\rho_{\text{sat}} = \frac{m_\phi}{\langle\sigma_{\phi\phi}v\rangle t_{\text{BH}}}, \quad (4.4)$$

where $v \sim 10^{-3}c$ is the thermal average velocity of the DM, t_{BH} is the age of the central black hole. We adopt nonself conjugate $\phi\phi^*$ annihilation cross section $\sigma_{\phi\phi}$, and their expression is included in Appendix A. For $r > R_{\text{sp}}$, it recovers the Navarro-Frenk-White (NFW) profile

$$\rho_{\text{NFW}} = \rho_0 \left(\frac{r}{r_0} \right)^{-\gamma} \left(1 + \frac{r}{r_0} \right)^{-(3-\gamma)}. \quad (4.5)$$

Taking $\gamma = 1$, we have $\gamma_{\text{sp}} = \frac{9-2\gamma}{4-\gamma} = \frac{7}{3}$, $g_\gamma(r) \simeq (1 - \frac{4R_s}{r})^3$, and

$$f(r) = r^{-\gamma_{\text{sp}}} \left(\frac{r^3}{3 - \gamma_{\text{sp}}} + \frac{12R_s r^2}{\gamma_{\text{sp}} - 2} - \frac{48R_s^2 r}{\gamma_{\text{sp}} - 1} + \frac{64R_s^3}{\gamma_{\text{sp}}} \right). \quad (4.6)$$

The DM density profile then follows [20]

$$\rho_{\text{DM}}(r) = \begin{cases} 0 & , r \leq 4R_s, \\ \frac{\rho_{\text{sp}}(r)\rho_{\text{sat}}}{\rho_{\text{sp}}(r) + \rho_{\text{sat}}} & , 4R_s \leq r \leq R_{\text{sp}}, \\ \frac{\rho_{\text{NFW}}(r)\rho_{\text{sat}}}{\rho_{\text{NFW}}(r) + \rho_{\text{sat}}} & , r \geq R_{\text{sp}}. \end{cases} \quad (4.7)$$

Since the distance between NGC 1068 and the Earth is around 14.4 Mpc, the effect of redshift is negligible. The estimates of NGC 1068 supermassive black hole vary, and we

adopt mass $M_{\text{BH}} \simeq 10^7 M_{\odot}$, age $t_{\text{BH}} \simeq 10^9$ yrs, and influence radius $r_h = 6.5 \times 10^5 R_s$ [20]. The optical depth of the emitted high-energy neutrinos is obtained via integrating the DM number density along the line of sight from $r = 4R_s$

$$\tau = \sigma_{\nu\phi} \int_{4R_s}^{14.4 \text{ Mpc}} \frac{\rho_{\text{DM}}(r)}{m_{\phi}} dr. \quad (4.8)$$

The NGC 1068 produces neutrinos with an energy interval $[E_{\text{min}}, E_{\text{max}}] = [1.5 \text{ TeV}, 15 \text{ TeV}]$, which is much larger than the mass range of ϕ that we considered for DSNB and DUNE. For AGNs emitting high-energy neutrinos, we adopt the kinematic region and parametrize cross section from Eq. (2.5), which is linear in E_{ν} , to compute the optical depth. Then Eq.(4.8) becomes

$$\tau = \sigma_{\nu\phi} \int_{4R_s}^{14.4 \text{ Mpc}} \frac{\rho_{\text{DM}}(r)}{m_{\phi}} dr = \frac{y^4 E_{\nu}}{32\pi m_F^4} \int_{4R_s}^{14.4 \text{ Mpc}} \rho_{\text{DM}}(r) dr. \quad (4.9)$$

The NGC 1068 neutrino flux is measured by the IceCube collaboration in terms of power law spectrum $\Phi(E_{\nu}) \propto (E_{\nu})^{-\hat{\gamma}}$ with the best fit value $\hat{\gamma} = 3.2$ [15]. Assuming no DM attenuation, we associate the N , measured events at IceCube, with NGC 1068 neutrino flux via [22]

$$N = t \int_{E_{\text{min}}}^{E_{\text{max}}} A_{\text{eff}}(E_{\nu}) \Phi(E_{\nu}) dE_{\nu}, \quad (4.10)$$

where t is the exposure time, A_{eff} is the effective area of the IceCube detector [20]. To compare with the event numbers influenced by $\nu\phi$ scattering and to give the constraints on m_{ϕ} and σ_0 , we require the following inequality:

$$\frac{N_{\text{sct}}}{N} = \frac{\int_{E_{\text{min}}}^{E_{\text{max}}} A_{\text{eff}}(E_{\nu}) \Phi(E_{\nu}) e^{-\tau(E_{\nu})} dE_{\nu}}{\int_{E_{\text{min}}}^{E_{\text{max}}} A_{\text{eff}}(E_{\nu}) \Phi(E_{\nu}) dE_{\nu}} \geq Q. \quad (4.11)$$

N_{sct} is the event number with $\nu\phi$ scattering included. We set $Q = 0.5$ and the corresponding constraint is shown in the right panel of Fig. 3. Four benchmark points are chosen on the NGC constraint, and the corresponding DM density profiles are shown in the left panel of Fig. 3. It shows that when m_{ϕ} is light enough, i.e. **NGC BP1**, the DM annihilation is negligible. Whereas, when m_{ϕ} is larger than 1 MeV, i.e. **NGC BP2** to **NGC BP4**, the $\phi\phi^*$ annihilation cross section $\sigma_{\phi\phi^*}$ becomes significant to alleviate the saturation density, hence the σ_0 must increase to compensate the deficit in the DM density, which causes the raising of solid-red curve in right panel of Fig. 3.

Another interesting AGN is the TXS 0506+056. It is a much more distant neutrino source than NGC 1068. Its redshift is measured as $z = 0.336$ [30] and corresponding distance is around 1.37 Gpc away from Earth. The relevant parameters for TXS 0506+056 are given by $r_i = 4R_s$, $r_h \simeq 10^5 R_s$, $M_{\text{BH}} \simeq 3.09 \times 10^8 M_{\odot}$, and $t_{\text{BH}} = 10^9$ years [31]. For ρ_0 and r_0 , they can be computed by $\rho_0 = 0.154 \text{ GeV/cm}^3$, $r_0 = 42.36 \text{ kpc}$ (see Appendix C for more details). Because of the cosmological distance of TXS 0506+056, we need to include the effect of cosmological expansion. From Eq. (2.6) and (4.9) we have,

$$\tau(E_{\nu}, 0.336) = \frac{y^4 E_{\nu}}{32\pi m_F^4} \int_0^{0.336} \frac{\rho_{\text{DM}}(d_0 - d(z))(1+z)^3}{H(z)} dz, \quad (4.12)$$

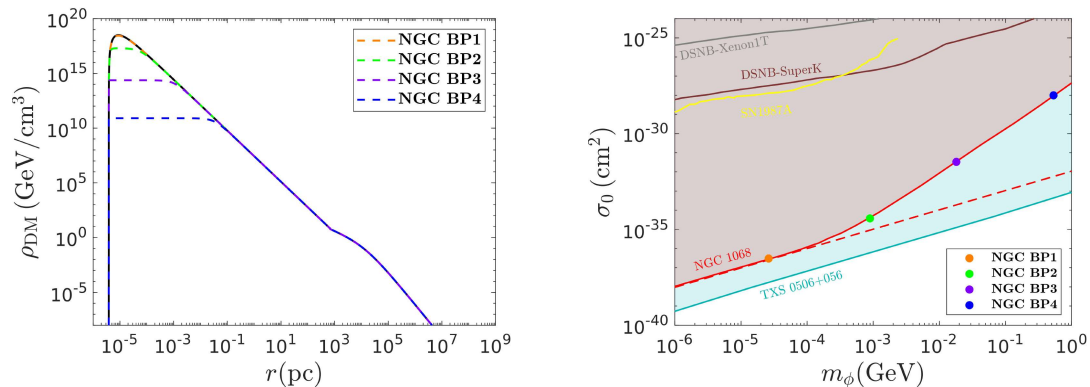


Figure 3: (left) The DM density profile of NGC 1068 with $\rho_0 = 0.35 \text{ GeV/cm}^3$, $M_{\text{BH}} = 10^7 M_{\odot}$, $r_0 = 13 \text{ kpc}$, $t_{\text{BH}} = 10^9 \text{ years}$, $r_h = 6.5 \times 10^5 R_s$, $r_i = 4R_s$. The black-solid curve depicts the density without $\phi\phi^*$ annihilation; the dashed curves are the modified densities of the **NGC BPs**'. The corresponding values of **NGC BPs** are listed in Table 2. (right) The constraints on σ_0 defined in Eq. (2.5) by requiring $Q = 0.5$, $m_F = 10 \text{ TeV}$, and $E_0 = 10 \text{ TeV}$. The solid-red curve is the constraint for NGC 1068, and the cyan for TXS 0506+056. The dashed line represents the constraint from NGC 1068 without $\phi\phi^*$ annihilation. For comparison, we also include the neutrino dark matter scattering bounds from DSNB-Xenon1T/SN1987A [20] and DSNB-SuperK [5].

where $d(z)$ is the comoving distance

$$d(z) = \int_0^z \frac{dz'}{H(z')} \quad (4.13)$$

and $d_0 = 1.37 \text{ Gpc}$. The main contribution of DM density is within the $R_{\text{sp}} (\sim 3.1 \text{ kpc})$, which is much smaller than d_0 . The redshifts for the density with $r \lesssim 1 \text{ Mpc}$ are nearly a constant, hence we approximate Eq. (4.12) by

$$\tau(E_\nu, 0.336) \simeq \frac{y^4 E_\nu}{32\pi m_F^4} (1.336)^3 \int_{4R_s}^R \rho_{\text{DM}} dr, \quad (4.14)$$

where the upper limit R is taken to be $R = 2 \text{ Mpc}$, and $\rho_{\text{DM}}(R) \simeq 1 \times 10^{-6} \text{ GeV/cm}^3$ is consistent with the average DM density in the extragalactic medium. The contribution for $r > R$ is negligible.

The effective area for IceCube can be parameterized as in Ref. [31], and the best fit power of neutrino flux for TXS 0506+056 is $\hat{\gamma} = 2$ [22]. The energy range of the neutrinos produced from TXS 0506+056 is $[E_{\text{min}}, E_{\text{max}}] = [40 \text{ TeV}, 4000 \text{ TeV}]$. We calculate the constraint on σ_0 for TXS 0506+056 according to Eq.(4.10) and Eq.(4.11), which reduces half of the events. Fig. 3 shows that the constraint for TXS 0506+056 is stronger than that of NGC 1068, this is because cross section $\sigma_{\nu\phi}$ is proportional to E_ν , and the neutrino energy is much higher of TXS 0506+056. Therefore, the coupling constant y must be smaller to prevent the intense scattering (N_{sct} must not be less than $0.5N$). Due to the smallness value of y , $\phi\phi^*$ annihilation has insignificant contribution in this case.

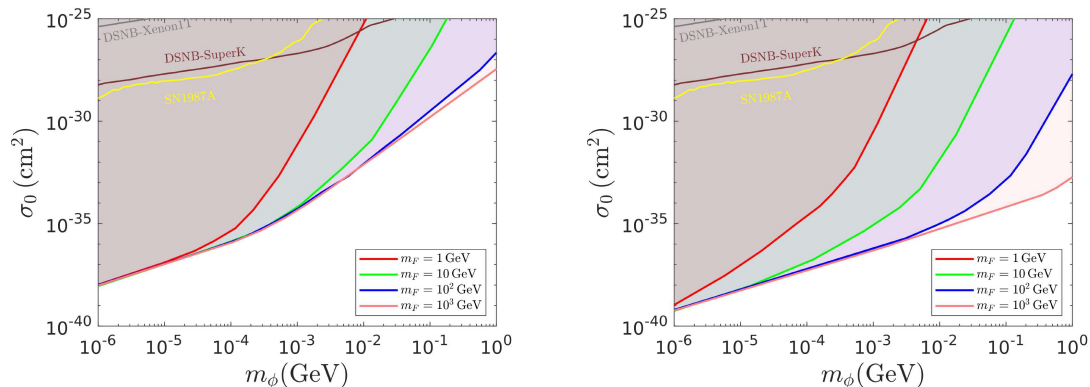


Figure 4: The constraints on σ_0 defined in Eq.(2.5) with $Q = 0.5$ and $E_0 = 10$ TeV, varying $m_F = 1$ GeV, 10 GeV, 100 GeV, 1000 GeV. Left (Right) panel is for NGC 1068 (TXS 0506+056).

We also calculated the constraints of σ_0 without assuming $m_F \gg m_\phi$ for comparison. In this case, we use the exact scattering cross section Eq. (A.4) and consider m_F from 1 GeV to 1000 GeV. In Fig. 4, we plot σ_0 against m_ϕ with various m_F and compare the results in Fig. 3 which fixes $m_F = 10$ TeV. For NGC 1068, the behaviors of these curves at low m_ϕ ($m_F \gg m_\phi$ still holds) are the same; the DM annihilation is irrelevant and the parameterized cross section Eq. (2.5) is still valid. As m_ϕ gets larger, the annihilation starts to contribute. When m_ϕ is large enough, such as $m_\phi E_\nu > m_F^2$ in the denominator of Eq. (A.8), the scattering cross section is proportional to E_ν^{-1} , and thus y must be drastically increased to satisfy $N_{\text{sct}}/N \leq 0.5$, which is shown in Fig. 4. For TXS 0506+056, when $m_F \gg m_\phi$ the scattering cross section is still proportional to E_ν , so the constraint curve remains lower than the one of NGC 1068. In the right panel of Fig. 4, since the energy range of TXS-emitted neutrinos is much larger than that of NGC, the condition $m_\phi E_\nu > m_F^2$ and the $\sigma_{\nu\phi}$ converting into E_ν^{-1} dependent occur at lighter m_ϕ comparing to the NGC one in the left panel. Due to the same reason, when m_F is getting lighter, the upper bounds of σ_0 of TXS deviate faster from the one with $m_F = 10$ TeV than those of NGC do.

5 Conclusion

We utilize two energy-distinctive astrophysical neutrino sources, DSNB and AGN, to constrain on the neutrino-DM interaction which is induced via exchanging a fermionic mediator. Given this, the neutrino-DM cross section exhibits different energy dependence in various kinematic parameter regions. Considering the attenuation on the neutrino flux during propagation, we derive the upper bounds of the coupling constant y and scattering cross section $\sigma_{\nu\phi}$. For $\mathcal{O}(10$ MeV) neutrino from DSNB, we calculate the optical depth and estimate the event numbers at DUNE detector through ν Ar scattering, then perform the chi-square test to find the upper bound of y as function of m_ϕ . Fig. 2 shows that the upper bound of y is small enough for the parameter region $E_\nu \gg m_\phi \simeq m_F$ and $\sigma_{\nu\phi} \propto E_\nu^{-1}$,

so that the amplitude satisfies perturbativity condition. Meanwhile, within the energy range $10.8 \leq E_\nu/\text{MeV} \leq 26.4$, the benchmark points in Table 1 predict the detectable attenuation of DSNB fluxes.

AGNs, NGC 1068 and TXS 0506+056, are the second sources we considered. The energy of neutrinos emitted from these two AGNs are much higher than those of DSNB, we thus focus on the kinematic region, $m_F^2 \gg E_\nu m_\phi \gg m_\phi^2$, such that $\sigma_{\nu\phi} \propto E_\nu$. Including the spike DM density profile around AGN supermassive black hole, the $\nu\phi$ scattering and the $\phi\phi^*$ annihilation cross sections both modify the neutrino flux at IceCube detector. Fig. 3 shows that both NGC 1068 and TXS 0506+056 can provide more stringent constraints than the DSNB-Xenon1T and SuperK. For NGC 1068, due to the fact that the DM annihilation becomes significant enough to suppress the saturation density when $m_\phi/\text{GeV} \gtrsim 10^{-4}$ the slope of σ_0 upper bound grows steeper. In particular, σ_0 takes the value from $1.1 \times 10^{-38} \text{ cm}^2$ to $1.2 \times 10^{-36} \text{ cm}^2$ for $10^{-6} \leq m_\phi/\text{GeV} \leq 10^{-4}$ and grows from $1.2 \times 10^{-36} \text{ cm}^2$ to $4.4 \times 10^{-28} \text{ cm}^2$ for $10^{-4} \leq m_\phi/\text{GeV} \leq 1$ in which the annihilation starts influence. Conversely, the annihilation is negligible for TXS 0506+056 due to its extremely high-energy neutrinos, since the coupling constant y must be reduced to compensate the intense $\nu\phi$ scattering. As a result, σ_0 maintains the linearity from $5.3 \times 10^{-40} \text{ cm}^2$ to $8.6 \times 10^{-34} \text{ cm}^2$ for $10^{-6} \leq m_\phi/\text{GeV} \leq 1$. If we decrease the value of m_F , as shown in Fig. 4, σ_0 increases when the condition $m_F \gg m_\phi$ breaks down. This is the direct consequence of the inverse proportionality between the exact cross section Eq.(A.8) and the neutrino energy, i.e. $\sigma_{\nu\phi} \propto 1/E_\nu$. For both NGC 1068 and TXS 0506+056, with $m_F = 1 \text{ GeV}$ and $m_\phi \gtrsim 5 \text{ MeV}$, the upper bound is getting even weaker than DSNB-SuperK.

Acknowledgment

P. Y. Tseng is supported in part by the National Science and Technology Council with Grant No. NSTC-111-2112-M-007-012-MY3. Y. M. Yeh is supported in part by Grant No. 113J0073I4 and Technology Council with Grant No. 111B3002I4.

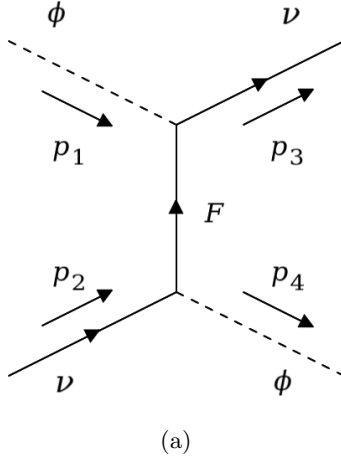


Figure 5

A Calculation of Cross Section

For the interaction (2.1), the amplitude is given by [21]

$$\sum_{s_2, s_3} |\mathcal{M}|^2 = \frac{4y^4}{(t - m_F)^2} \left[(p_1 \cdot p_2)(p_1 \cdot p_3) - \frac{m_\phi^2}{2}(p_2 \cdot p_3) \right] = \frac{y^4(m_\phi^4 - st)}{(t - m_F^2)^2} \quad (\text{A.1})$$

and the Feynman diagram is shown in Fig. 5. The Mandelstam variable t is given by

$$t = \frac{2sm_\phi^2 - s^2 + m_\phi^4}{2s} - \frac{(s - m_\phi^2)^2}{2s} \cos \theta \equiv A - B \cos \theta, \quad (\text{A.2})$$

where θ is the scattering angle in the CM frame. Then (A.1) becomes

$$\sum_{s_2, s_3} |\mathcal{M}|^2 = \frac{y^4[m_\phi^4 - s(A - B \cos \theta)]}{(A - m_F^2 - B \cos \theta)^2}. \quad (\text{A.3})$$

The cross section is

$$\sigma_{\nu\phi} = \frac{I}{64\pi^2 s}, \quad (\text{A.4})$$

where

$$I = \int d\Omega \left\langle \sum_{s_2, s_3} |\mathcal{M}|^2 \right\rangle = y^4 \pi \left\{ \frac{s[(m_F^2 - A)^2 - B^2] \ln \left(\left| \frac{m_F^2 + B - A}{m_F^2 - B - A} \right| \right) + 2B(m_\phi^4 - sm_F^2)}{B[(m_F^2 - A)^2 - B^2]} \right\}. \quad (\text{A.5})$$

The neutrinos from the AGN have energy of TeV scale, which is much greater than the DM mass m_ϕ , thus in the ϕ rest frame

$$s = m_\phi^2 + 2E_\nu m_\phi \simeq 2E_\nu m_\phi, \quad A \simeq -E_\nu m_\phi \simeq -B \quad (\text{A.6a})$$

In this case (A.5) can be approximated by

$$I \simeq 2y^4 \pi \left[\ln \left(1 + \frac{2E_\nu m_\phi}{m_F^2} \right) - \frac{2E_\nu m_\phi}{m_F^2 + 2E_\nu m_\phi} \right] \quad (\text{A.7})$$

and the corresponding cross section is

$$\sigma_{\nu\phi} = \frac{y^4}{32\pi} \left[\frac{\ln\left(1 + \frac{2E_\nu m_\phi}{m_F^2}\right)}{2E_\nu m_\phi} - \frac{1}{m_F^2 + 2E_\nu m_\phi} \right]. \quad (\text{A.8})$$

In our analysis, we set $m_F \geq 1$ TeV and $m_F^2 \gg E_\nu m_\phi$. The cross section then becomes linear in E_ν :

$$\sigma_{\nu\phi} = \left(\frac{y^4 m_\phi}{32\pi m_F^4} \right) E_\nu. \quad (\text{A.9})$$

As For the $\phi\phi^*$ annihilation, we consider the nonself conjugate scalar DM annihilation, the corresponding amplitude is given by [21]

$$\int_{-1}^1 |\mathcal{M}|^2 d\cos\theta = \frac{16y^4 |\mathbf{p}_i|^2 m_\phi^2}{3(m_F^2 + m_\phi^2)^2}. \quad (\text{A.10})$$

So the total cross section is

$$\sigma_{\phi\phi} = \frac{1}{32\pi s} \frac{|\mathbf{p}_f|}{|\mathbf{p}_i|} \int_{-1}^1 |\mathcal{M}|^2 d\cos\theta. \quad (\text{A.11})$$

The amplitude of initial and final three momentum $|\mathbf{p}_i|$ is

$$|\mathbf{p}_i| = m_\phi \gamma \langle v \rangle, \quad |\mathbf{p}_f| = \sqrt{m_\phi^2 \gamma^2 - m_\nu^2} \quad (\text{A.12})$$

with $\gamma = (1 - \langle v \rangle^2)^{-1/2}$, $s = (2m_\phi \gamma)^2$.

B The Detail Calculation of ν Ar Scattering

The cross section of the charged current ν_e ^{40}Ar scattering is given by

$$\sigma_{\nu\text{Ar}} = \frac{G_F^2 |V_{ud}|^2 E_e^{\text{CM}} |\mathbf{p}_e^{\text{CM}}|}{\pi} \left[\frac{(\sqrt{s} - E_e^{\text{CM}}) E_{\text{Ar}}^{\text{CM}}}{s} \right] F_C [B(\text{F}) + B(\text{GT})], \quad (\text{B.1})$$

where $G_F = 1.17 \times 10^{-5} \text{ GeV}^{-2}$ is the Fermi constant, V_{ud} is the CKM matrix element connecting the up and down quarks. F_C is the allowed approximation Coulomb correction factor [27]

$$F_C = \begin{cases} F(Z_f, v_{\text{rel}}), & f_{\text{EMA}}^2 > F(Z_f, v_{\text{rel}}) \\ f_{\text{EMA}}^2, & \text{otherwise} \end{cases}, \quad (\text{B.2})$$

where

$$F(Z_f, E_e^{\text{FNR}}) = \frac{2(1+S)}{[\Gamma(1+2S)]^2} (2|\mathbf{p}_e^{\text{FNR}}|R)^{2S-2} e^{-\pi\eta} |\Gamma(S+i\eta)|^2 \quad (\text{B.3})$$

is the Fermi function in the "final nucleus rest frame" (FNR frame). We transform the four momenta in the CM frame into the FNR frame. In the CM frame, the four momentum of e^- and ^{40}K are $p_e = (E_e^{\text{CM}}, \mathbf{p}_e^{\text{CM}})$ and $p_K = (E_K^{\text{CM}}, -\mathbf{p}_e^{\text{CM}})$ with

$$E_e^{\text{CM}} = \frac{s + m_e^2 - m_K^2}{2\sqrt{s}}, \quad E_K^{\text{CM}} = \frac{s - m_e^2 + m_K^2}{2\sqrt{s}}. \quad (\text{B.4})$$

In the FNR frame, ^{40}K is at rest, so

$$\mathbf{p}_K^{\text{FNR}} \hat{\mathbf{x}} = \gamma(-|\mathbf{p}_e^{\text{CM}}| - E_K^{\text{CM}} v) \hat{\mathbf{x}} = \mathbf{0}, \quad (\text{B.5})$$

where $\hat{\mathbf{x}}$ is the direction of electron. This yields $v = -|\mathbf{p}_e^{\text{CM}}|/E_K^{\text{CM}}$. The four momentum of electron in FNR frame is

$$\begin{aligned} \mathbf{p}_e^{\text{FNR}} \hat{\mathbf{x}} &= \gamma \left(|\mathbf{p}_e^{\text{CM}}| + E_e^{\text{CM}} \frac{|\mathbf{p}_e^{\text{CM}}|}{E_K^{\text{CM}}} \right) \hat{\mathbf{x}} = \gamma |\mathbf{p}_e^{\text{CM}}| \left(1 + \frac{E_e^{\text{CM}}}{E_K^{\text{CM}}} \right) \hat{\mathbf{x}}, \\ E_e^{\text{FNR}} &= \gamma \left(E_e^{\text{CM}} + |\mathbf{p}_e^{\text{CM}}| \frac{|\mathbf{p}_e^{\text{CM}}|}{E_K^{\text{CM}}} \right) = \gamma \left(E_e^{\text{CM}} + \frac{|\mathbf{p}_e^{\text{CM}}|^2}{E_K^{\text{CM}}} \right). \end{aligned} \quad (\text{B.6})$$

The relative velocity of electron to the rest K is then $v_{\text{rel}} = \mathbf{p}_e^{\text{FNR}}/E_e^{\text{FNR}}$, and the Lorentz factor is $\gamma_{\text{rel}} = E_e^{\text{FNR}}/m_e$. Hence we may write (B.3) as

$$F(Z_f, v_{\text{rel}}) = \frac{2(1+S)}{[\Gamma(1+2S)]^2} (2\gamma_{\text{rel}} v_{\text{rel}} m_e R)^{2S-2} e^{-\pi\eta} |\Gamma(S+i\eta)|^2. \quad (\text{B.7})$$

The velocity of the CM frame observed from the lab (Ar rest) frame is given by

$$v_{\text{CM}} = \frac{p_{\nu x}}{E_\nu + m_{\text{Ar}}} = \frac{|\mathbf{p}_\nu|}{E_\nu + m_{\text{Ar}}} \quad (\text{B.8})$$

and

$$\gamma_{\text{CM}} = \frac{1}{\sqrt{1-v_{\text{CM}}^2}} = \frac{m_{\text{Ar}} + E_\nu}{\sqrt{m_{\text{Ar}}^2 + 2m_{\text{Ar}}E_\nu}}. \quad (\text{B.9})$$

The Mandelstam variable s in the lab frame is

$$s = m_{\text{Ar}}^2 + 2E_\nu m_{\text{Ar}}. \quad (\text{B.10})$$

With (B.10) and (B.4) we can write E_e^{CM} , $|\mathbf{p}_e^{\text{CM}}|$ in terms of masses and E_ν , and $E_{\text{Ar}}^{\text{CM}} = \gamma_{\text{CM}} m_{\text{Ar}}$.

f_{EMA} is the rescaled factor of effective momentum approximation (EMA) and is given by

$$f_{\text{EMA}} = \frac{|\mathbf{p}_e^{\text{eff}}|}{|\mathbf{p}_e|}, \quad (\text{B.11})$$

where

$$|\mathbf{p}_e^{\text{eff}}| = \sqrt{\left(E_e + \frac{3Z_f \alpha}{2R} \right)^2 - m_e^2}. \quad (\text{B.12})$$

C Calculation for ρ_0 and r_0

We follow the formula in [32], the characteristic radius and density of the distribution are given by

$$\rho_0 = \frac{\Delta}{3} \frac{c^3}{\ln(1+c) - \frac{c}{1+c}} \rho_c, \quad r_0 \simeq 8.8 \left(\frac{M_{\text{vir}}}{10^{11} M_\odot} \right)^{0.46} \text{ kpc} \quad (\text{C.1})$$

where $\Delta = 200$ is the virial overdensity and

$$\rho_c = 1.053672 \times 10^{-5} h^2 (\text{GeV}/c^2)\text{cm}^{-3} \simeq 4.78658 \times 10^{-6} (\text{GeV}/c^2)\text{cm}^{-3}, \quad (\text{C.2a})$$

$$c \simeq 13.6 \left(\frac{M_{\text{vir}}}{10^{11} M_{\odot}} \right)^{-0.13} \quad (\text{C.2b})$$

are the critical density of the universe and concentration parameter. The DM halo mass is related to the central supermassive black hole mass by [20]

$$M_{\text{DM}} \sim 10^{12} M_{\odot} \times \left(\frac{M_{\text{BH}}}{7 \times 10^7 M_{\odot}} \right)^{3/4}. \quad (\text{C.3})$$

We take the DM halo mass to be the virial mass, then we have

$$\begin{aligned} M_{\text{DM}} &\simeq 2.32 \times 10^{11} M_{\odot} \quad (\text{NGC}), \\ M_{\text{DM}} &\simeq 3.05 \times 10^{12} M_{\odot} \quad (\text{TXS}), \end{aligned} \quad (\text{C.4})$$

and from (C.1)-(C.2) we have

$$\begin{aligned} \rho_0 &\simeq 0.35 \text{ GeV}/\text{cm}^3, \quad r_0 \simeq 13 \text{ kpc} \quad (\text{NGC}), \\ \rho_0 &\simeq 0.154 \text{ GeV}/\text{cm}^3, \quad r_0 \simeq 42.36 \text{ kpc} \quad (\text{TXS}). \end{aligned} \quad (\text{C.5})$$

References

- [1] G. Mangano, A. Melchiorri, P. Serra, A. Cooray, and M. Kamionkowski, ‘‘Cosmological bounds on dark matter-neutrino interactions’’, *Phys. Rev. D* **74** (2006) 043517, [astro-ph/0606190](#).
- [2] I. R. Wang and X.-J. Xu, ‘‘Imprints of light dark matter on the evolution of cosmic neutrinos’’, *JCAP* **05** (2024) 050, [arXiv:2312.17151](#).
- [3] D. C. Hooper and M. Lucca, ‘‘Hints of dark matter-neutrino interactions in Lyman- α data’’, *Phys. Rev. D* **105** (2022), no. 10, 103504, [arXiv:2110.04024](#).
- [4] **IceCube** Collaboration, A. McMullen, A. Vincent, C. Arguelles, and A. Schneider, ‘‘Dark matter neutrino scattering in the galactic centre with IceCube’’, *JINST* **16** (2021), no. 08, C08001, [arXiv:2107.11491](#).
- [5] D. Ghosh, A. Guha, and D. Sachdeva, ‘‘Exclusion limits on dark matter-neutrino scattering cross section’’, *Phys. Rev. D* **105** (2022), no. 10, 103029, [arXiv:2110.00025](#).
- [6] Y. Zhang, ‘‘Speeding up dark matter with solar neutrinos’’, *PTEP* **2022** (2022), no. 1, 013B05, [arXiv:2001.00948](#).
- [7] Y. Jho, J.-C. Park, S. C. Park, and P.-Y. Tseng, ‘‘Cosmic-Neutrino-Boosted Dark Matter (νBDM)’’, [arXiv:2101.11262](#).
- [8] K. Agashe, Y. Cui, L. Necib, and J. Thaler, ‘‘(In)direct Detection of Boosted Dark Matter’’, *JCAP* **10** (2014) 062, [arXiv:1405.7370](#).
- [9] J. F. Beacom, ‘‘The Diffuse Supernova Neutrino Background’’, *Ann. Rev. Nucl. Part. Sci.* **60** (2010) 439–462, [arXiv:1004.3311](#).

- [10] S. Horiuchi, J. F. Beacom, and E. Dwek, “The Diffuse Supernova Neutrino Background is detectable in Super-Kamiokande”, *Phys. Rev. D* **79** (2009) 083013, [arXiv:0812.3157](#).
- [11] A. De Gouvêa, I. Martinez-Soler, Y. F. Perez-Gonzalez, and M. Sen, “Fundamental physics with the diffuse supernova background neutrinos”, *Phys. Rev. D* **102** (2020) 123012, [arXiv:2007.13748](#).
- [12] **Super-Kamiokande** Collaboration, H. Zhang *et al.*, “Supernova Relic Neutrino Search with Neutron Tagging at Super-Kamiokande-IV”, *Astropart. Phys.* **60** (2015) 41–46, [arXiv:1311.3738](#).
- [13] **DUNE** Collaboration, B. Abi *et al.*, “Deep Underground Neutrino Experiment (DUNE), Far Detector Technical Design Report, Volume I Introduction to DUNE”, *JINST* **15** (2020), no. 08, T08008, [arXiv:2002.02967](#).
- [14] **DUNE** Collaboration, B. Abi *et al.*, “Deep Underground Neutrino Experiment (DUNE), Far Detector Technical Design Report, Volume II: DUNE Physics”, [arXiv:2002.03005](#).
- [15] **IceCube** Collaboration, R. Abbasi *et al.*, “Evidence for neutrino emission from the nearby active galaxy NGC 1068”, *Science* **378** (2022), no. 6619, 538–543, [arXiv:2211.09972](#).
- [16] **IceCube** Collaboration, M. G. Aartsen *et al.*, “Neutrino emission from the direction of the blazar TXS 0506+056 prior to the IceCube-170922A alert”, *Science* **361** (2018), no. 6398, 147–151, [arXiv:1807.08794](#).
- [17] **IceCube, Fermi-LAT, MAGIC, AGILE, ASAS-SN, HAWC, H.E.S.S., INTEGRAL, Kanata, Kiso, Kapteyn, Liverpool Telescope, Subaru, Swift NuSTAR, VERITAS, VLA/17B-403** Collaboration, M. G. Aartsen *et al.*, “Multimessenger observations of a flaring blazar coincident with high-energy neutrino IceCube-170922A”, *Science* **361** (2018), no. 6398, eaat1378, [arXiv:1807.08816](#).
- [18] P. Gondolo and J. Silk, “Dark matter annihilation at the galactic center”, *Phys. Rev. Lett.* **83** (1999) 1719–1722, [astro-ph/9906391](#).
- [19] G. Herrera and K. Murase, “Probing Light Dark Matter through Cosmic-Ray Cooling in Active Galactic Nuclei”, [arXiv:2307.09460](#).
- [20] J. M. Cline and M. Puel, “NGC 1068 constraints on neutrino-dark matter scattering”, *JCAP* **06** (2023) 004, [arXiv:2301.08756](#).
- [21] C. Boehm and P. Fayet, “Scalar dark matter candidates”, *Nucl. Phys. B* **683** (2004) 219–263, [hep-ph/0305261](#).
- [22] C. Döring and S. Vogl, “Astrophysical neutrino point sources as a probe of new physics”, [arXiv:2304.08533](#).
- [23] A. Das and M. Sen, “Boosted dark matter from diffuse supernova neutrinos”, *Phys. Rev. D* **104** (2021), no. 7, 075029, [arXiv:2104.00027](#).
- [24] **Planck** Collaboration, N. Aghanim *et al.*, “Planck 2018 results. VI. Cosmological parameters”, *Astron. Astrophys.* **641** (2020) A6, [arXiv:1807.06209](#), [Erratum: *Astron. Astrophys.* 652, C4 (2021)].
- [25] H. Yuksel, M. D. Kistler, J. F. Beacom, and A. M. Hopkins, “Revealing the High-Redshift Star Formation Rate with Gamma-Ray Bursts”, *Astrophys. J. Lett.* **683** (2008) L5–L8, [arXiv:0804.4008](#).

- [26] E. E. Salpeter, “The Luminosity function and stellar evolution”, *Astrophys. J.* **121** (1955) 161–167.
- [27] S. J. Gardiner, “Nuclear Effects in Neutrino Detection”, PhD thesis, UC, Davis, 2018.
- [28] A. de Gouvêa, I. Martinez-Soler, Y. F. Perez-Gonzalez, and M. Sen, “Diffuse supernova neutrino background as a probe of late-time neutrino mass generation”, *Phys. Rev. D* **106** (2022), no. 10, 103026, [arXiv:2205.01102](#).
- [29] O. Y. Gnedin and J. R. Primack, “Dark Matter Profile in the Galactic Center”, *Phys. Rev. Lett.* **93** (2004) 061302, [astro-ph/0308385](#).
- [30] S. Paiano, R. Falomo, A. Treves, and R. Scarpa, “The redshift of the BL Lac object TXS 0506+056”, *Astrophys. J. Lett.* **854** (2018), no. 2, L32, [arXiv:1802.01939](#).
- [31] J. M. Cline, S. Gao, F. Guo, Z. Lin, S. Liu, M. Puel, P. Todd, and T. Xiao, “Blazar Constraints on Neutrino-Dark Matter Scattering”, *Phys. Rev. Lett.* **130** (2023), no. 9, 091402, [arXiv:2209.02713](#).
- [32] G. Gentile, C. Tonini, and P. Salucci, “Lambda CDM Halo Density Profiles: Where do actual halos converge to NFW ones?”, *Astron. Astrophys.* **467** (2007) 925–931, [astro-ph/0701550](#).
- [33] M. Klasen, M. Pohl, and G. Sigl, “Indirect and direct search for dark matter”, *Prog. Part. Nucl. Phys.* **85** (2015) 1–32, [arXiv:1507.03800](#).
- [34] J. Billard et al., “Direct detection of dark matter—APPEC committee report*”, *Rept. Prog. Phys.* **85** (2022), no. 5, 056201, [arXiv:2104.07634](#).
- [35] R. K. Leane, “Indirect Detection of Dark Matter in the Galaxy”, in “3rd World Summit on Exploring the Dark Side of the Universe”, pp. 203–228. 2020. [arXiv:2006.00513](#).
- [36] B. Carr and F. Kuhnel, “Primordial Black Holes as Dark Matter: Recent Developments”, *Ann. Rev. Nucl. Part. Sci.* **70** (2020) 355–394, [arXiv:2006.02838](#).
- [37] D. Marfatia and P.-Y. Tseng, “Correlated signals of first-order phase transitions and primordial black hole evaporation”, *JHEP* **08** (2022) 001, [arXiv:2112.14588](#), [Erratum: *JHEP* 08, 249 (2022)].
- [38] R. Calabrese, M. Chianese, D. F. G. Fiorillo, and N. Saviano, “Direct detection of light dark matter from evaporating primordial black holes”, *Phys. Rev. D* **105** (2022), no. 2, L021302, [arXiv:2107.13001](#).
- [39] M. Sasaki, T. Suyama, T. Tanaka, and S. Yokoyama, “Primordial black holes—perspectives in gravitational wave astronomy”, *Class. Quant. Grav.* **35** (2018), no. 6, 063001, [arXiv:1801.05235](#).